Aeroacoustic analysis of an airfoil with Gurney flap based on time-resolved particle image velocimetry measurements

Zhang, Xueqing; Sciacchitano, Andrea; Pröbsting, Stefan

DOI
10.1016/j.jsv.2018.02.039

Publication date
2018

Document Version
Final published version

Published in
Journal of Sound and Vibration

Citation (APA)
Zhang, X., Sciacchitano, A., & Pröbsting, S. (2018). Aeroacoustic analysis of an airfoil with Gurney flap based on time-resolved particle image velocimetry measurements. *Journal of Sound and Vibration*, *422*, 490-505. https://doi.org/10.1016/j.jsv.2018.02.039

Journal of Sound and Vibration 422 (2018) 490–505

Contents lists available at ScienceDirect

Journal of Sound and Vibration

journal homepage: www.elsevier.com/locate/jsvi

Aeroacoustic analysis of an airfoil with Gurney flap based on time-resolved particle image velocimetry measurements

Xueqing Zhang [a,*], Andrea Sciacchitano [b], Stefan Pröbsting [b]

[a] Mechanical and Mechatronics Engineering, University of Waterloo, 200 University Avenue West, N2L 3G1 Waterloo, ON, Canada
[b] Department of Aerodynamics, Delft University of Technology, Kluyverweg 2, 2629HT Delft, The Netherlands

ARTICLE INFO

Article history:
Received 4 February 2017
Revised 13 February 2018
Accepted 19 February 2018
Available online XXX

Keywords:
Time-resolved PIV
Gurney flap noise
Curle's aeroacoustic analysis

ABSTRACT

Particle image velocimetry for the experimental assessment of trailing edge noise sources has become focus of research in recent years. The present study investigates the feasibility of the noise prediction for high-lift devices based on time-resolved particle image velocimetry (PIV). The model under investigation is a NACA 0015 airfoil with a Gurney flap with a height of 6% of the chord length. The velocity fields around and downstream of the Gurney flap were measured by PIV and used to compute the corresponding pressure fields by solving the Poisson equation for incompressible flows. The reconstructed pressure fluctuations on the airfoil surface constitute the source term for Curle's aeroacoustic analogy, which was employed in both the distributed and compact formulation to estimate the noise emission from PIV. The results of the two formulations are compared with the simultaneous far-field microphone measurements in the temporal and spectral domains. Both formulations of Curle's analogy yield acoustic sound pressure levels in good agreement with the simultaneous microphone measurements for the tonal component. The estimated far-field sound power spectra (SPL) from the PIV measurements reproduce the peak at the vortex shedding frequency, which also agrees well with the acoustic measurements.

1. Introduction

With the implementation of large bypass ratio turbo-fan engines on civil aircraft, which remarkably reduce the level of engine noise, the attention of noise control has shifted to the reduction of airframe noise. The deployment of high-lift devices during takeoff and landing is one of the major sources of this type of aerodynamically generated noise [1]. Traditional approaches of acoustic assessment rely mainly on microphone (array) measurements (for instance Hutcheson and Brooks [2]) or instantaneous flow fields obtained from numerical CFD codes, such as URANS and LES (for instance Casalino et al. [3]). However, the former approach fails in providing the mechanism of noise generation, while the latter becomes prohibitive in the operating Reynolds number range of real aircraft.

A seminal paper in aeroacoustics, published in 1952 by M. J. Lighthill [4], established a mathematical relation between the unsteady flow field quantities and the radiated sound. 60 years later, with the rapid advancement in hardware and software in the past decade, PIV has become a powerful tool for capturing the instantaneous velocity field with a high combined spatial and temporal dynamic range when compared to other measurement methods. In recent years, the application of time-resolved PIV (TR-PIV) in aeroacoustic investigations became focus of interest. Henning et al. have performed a series of synchronized PIV and microphone measurements on a cylinder wake [5], rod-airfoil configuration [6], cold jet [7] and high-lift device [8] to identify the

* Corresponding author.
E-mail addresses: x634zhan@uwaterloo.ca (X. Zhang), a.sciacchitano@tudelft.nl (A. Sciacchitano), s.probsting@tudelft.nl (S. Pröbsting).

https://doi.org/10.1016/j.jsv.2018.02.039
0022-460X/

flow patterns responsible for the noise emission. Pröbsting et al. [9,10] have employed time-resolved PIV in combination with non-stationary signal processing for the analysis of the source field around an airfoil generating tonal noise. Noise predictions based on TR-PIV data have also been achieved in recent years. Haigermoser [11] derived the hydrodynamic pressure fluctuations in the far field of a cavity flow with Curle's analogy based on planar TR-PIV measurements in a water tunnel. Koschatzky et al. [12] applied Curle's analogy and vortex sound theory to the noise prediction of an open, two-dimensional shallow cavity. Lorenzoni et al. [13] investigated the acoustic emission from vortex-structure of a rod-airfoil configuration. More recently, Pröbsting et al. [14] demonstrated the prediction of broadband noise, caused by the interaction of the turbulent boundary layer with the trailing edge, based on time-resolved tomographic PIV. Shah et al. [15] employed simultaneous planar TR-PIV and far-field microphone measurements to identify the flow structures associated with Gurney flap that are highly correlated to noise emission.

PIV measurements provide the velocity fields in a two- or three-dimensional domain. The spatial gradients of the hydrodynamic pressure can be derived from the momentum equation. For 2D PIV measurements, the pressure field can be reconstructed either by direct spatial integration [16] or by solution of the Poisson equation obtained from taking the in-plane divergence of the momentum equation with appropriate boundary conditions [17]. The former method introduces an accumulation of random errors along the integration path. The omni-directional, virtual boundary integration scheme developed by Liu and Katz [18] enables integration with a reduced effect on the local random error. The accuracy of the pressure reconstruction involved in both approaches is strongly dependent upon the choice of the Lagrangian or Eulerian formulation of the velocity temporal derivatives. Violato et al. [19] compared the two formulations on a rod-airfoil configuration and offered guidelines for the choice of the experimental parameters (e.g. time separation between successive velocity fields) according to the approach adopted. De Kat and van Oudheusden [20] further assessed the experimental viability of the approaches in the reconstruction of instantaneous pressure field, giving emphasis to the flow features which are associated with the convecting vortices.

Under the assumption of incompressible flow, the aerodynamic loads can further be derived on the basis of pressure reconstruction with the momentum balanced equation proposed by Kurtulus et al. [21]. Alternatively, Noca et al. [22] derived and compared three methods for the evaluation of time-dependent forces circumventing the step of pressure reconstruction.

In the past, aeroacoustic analogies have been successfully applied only to very simple cases (e.g. cavity flow, cylinder) which have little interest in real aerospace applications. In the present work, the use of aeroacoustic analogies is extended to a problem relevant in the aerospace sector, that is the noise prediction of high-lift devices. The present study aims at investigating the feasibility of quantitative aeroacoustic prediction of lift-enhancing devices based on TR-PIV measurements, where the Gurney flap serves as a simplified model of the flaps typically employed in civil aviation. Two formulations of Curle's analogy are applied in the data reduction and the two predictions are compared respectively with the simultaneous far-field acoustic pressure recorded by the microphone. The outcome is a first step towards optical diagnostics of the aeroacoustic emissions due to the flow field around a high-lift device.

2. Experiments

2.1. Experimental facility and model

Simultaneous planar PIV and microphone measurements were carried out in the vertical low turbulence wind tunnel (V-tunnel) at Delft University of Technology. A circular-to-square transition flow duct was installed to accommodate a closed test section with exit dimensions of 40×40 cm^2. The test section for simultaneous PIV-microphone measurements consists of two side-plates made of plexi-glass for camera imaging, and two side-plates made of Kevlar, an acoustic transparent material [23], for microphone measurements (Fig. 3 (A–A)). A NACA 0015 model of $c = 20$ cm chord, wetted span of $L = 40$ cm and with a Gurney flap of $h = 12$ mm height (6% of the chord c) was placed vertically in the wind tunnel with its geometric angle of attack set to 4°. The detachable trailing edge of the model was made out of plexi-glass to allow the passage of laser light, such that the velocity field on both pressure and suction side of the trailing edge could be captured simultaneously. The boundary layer was tripped at the quarter-chord location with roughness elements of 0.84 mm nominal grain size. The configuration was examined at a nominal free stream velocity of 20 m $\cdot$ s^{-1} with an incoming turbulent level below 0.1%.

2.2. Flow field measurements

Two-component TR-PIV was used to obtain the planar velocity field around and downstream of the Gurney flap. The light sheet was placed at the mid-span section of the airfoil. The illumination was provided by a Quantronix Nd-YLF laser (2×12 mJ/pulse at 2.7 kHz) and the flow was seeded with water-glycol based fog with droplets with a median diameter of 1 μm.

For the reason of spatial resolution, two Photron Fastcam SA1.1 cameras (CMOS sensor, 1024×1024 pixels, 12-bit and pixel pitch 20 μm, 5.4 kHz acquisition frequency at full resolution in single-frame mode), placed facing each other on opposite sides of the test section, were used for image acquisition. To achieve a higher acquisition frequency of 5 kHz in frame-straddling mode, the sensors of the two cameras were cropped to 704×704 px^2. Each camera was equipped with a Nikon Micro-Nikkor 105 mm lens to capture a field of view (FOV) of 80×80 mm^2, resulting in a combined field of view of roughly 80×140 mm^2 (Fig. 1) and a magnification factor $M = 0.176$. Two settings of combined FOV were used to compare the effect of FOV on acoustic prediction, with FOV 1 ranging from $0.5c \leqslant y - y_{LE} \leqslant 1.2c$, and FOV 2 ranging from $0.8c \leqslant y - y_{LE} \leqslant 1.5c$. The aperture was set to $f_{\#} = 2.8$ to collect sufficient light. Under the setting of such a numerical aperture, the particle image diameter is around 0.2 px. To avoid

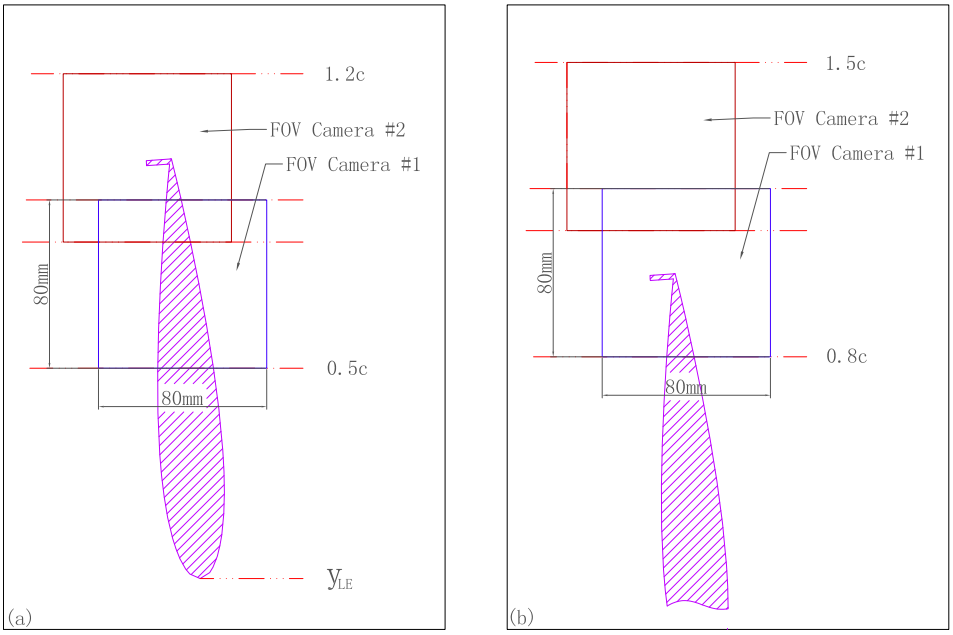

Fig. 1. Two settings of Field of View for two-camera recording: FOV1 (a) and FOV2 (b).

peak-locking errors [24], the focal plane of the cameras was slightly shifted with respect to the measurement plane to obtain a particle image diameter larger than 1 px.

The recording comprises 5773 image pairs acquired at a frequency of 5 kHz and with a laser pulse separation of 50 μs, corresponding to a displacement of 1 mm (approximately 9 pixels) in the free stream. The illumination and imaging system were synchronized with a LaVision High-Speed controller and the acquisition was controlled by the DaVis 8 software. The latter was also used for the image processing and interrogation.

The images were processed with sequential cross-correlation algorithm with multi-pass iterations of decreasing interrogation window sizes from 64×64, 50% overlap, to 32×32 to 75% overlap, Gaussian-weighted window. Vector post-processing was applied to remove the outliers. The spurious velocity vectors were detected by means of the normalized median test, developed by Westerweel and Scarano in 2005 [25].

A snapshot of the instantaneous visualization of the transverse (u-component) and streamwise (v-component) velocity fields around and downstream of the Gurney flap is provided by Fig. 2(a), (b). Velocity values were interpolated to the shadowed region in PIV experiments (marked by dashed lines) with nearest-neighbour interpolation to facilitate the pressure evaluation. The power spectra of the transverse velocity fluctuations in the near-wake is given in Fig. 2(c).

2.3. Acoustic measurements

The simultaneous acoustic measurements were performed by a set of four LinearX-M53 microphones, placed at a fixed distance of 1.3 m from the airfoil trailing edge, such that the microphones were in the far field with respect to the airfoil. The microphones were placed at angles, with respect to the horizontal line, of 30°, 18°, 0° and −18° respectively, as shown in Fig. 3. Table 1 gives an overview of the experimental parameters of the synchronized planar PIV and microphone measurements.

3. Data reduction procedures

3.1. Aeroacoustic model

Curle's analogy is a reformulation of the Navier Stokes equations, based on the assumptions of stationary, rigid and solid surfaces in the flow. Under the additional assumptions of high Reynolds and low Mach number, the contribution of viscous and quadrupole terms is negligible [26,27]. Following these simplifications, the acoustic pressure p_a at the listener's location $\mathbf{x}$ in the far field at time t is a direct consequence of the summation of the influence of pressure fluctuation p' distributed on the surface δV_y of the solid body submerged in the flow produced at time t_e in the source region and reaching the listener at time t. Here, the acoustic pressure p_a is defined as the deviation of the local pressure p from the equilibrium value p_0, namely, $p_a = p - p_0$. Since the pressure fluctuations propagate in a quiescent medium at the speed of sound, the retarded time t_e is related to t by c_0,

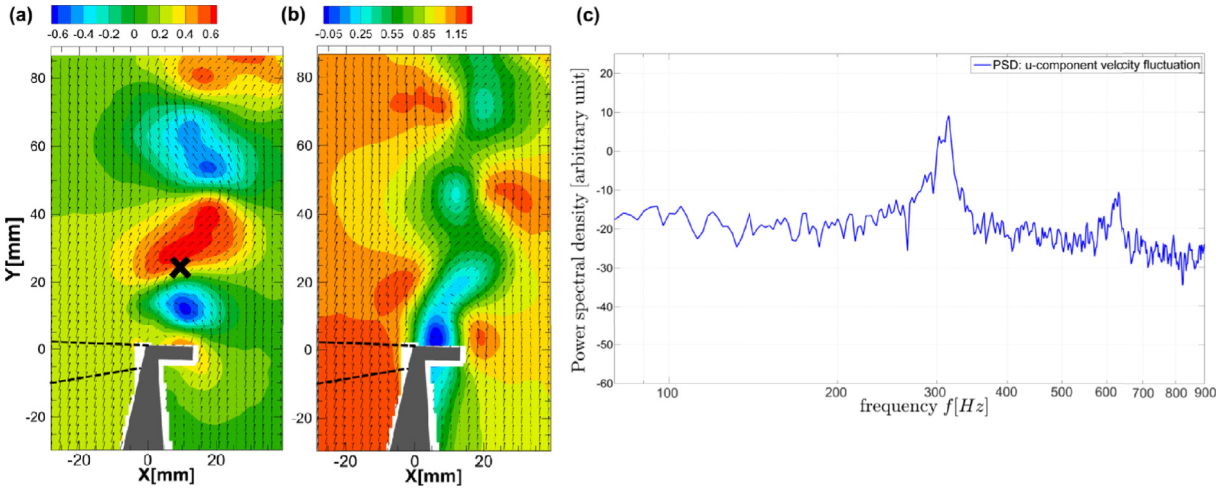

Fig. 2. A snapshot of the non-dimensionalized instantaneous transverse velocity (a) and streamwise velocity (b) evaluated from FOV2. Dashed lines indicate the shadowed region where velocity values were interpolated with nearest-neighbour interpolation. Power spectra of the transverse velocity fluctuations sampled at the cross location marked in (a) is given in (c).

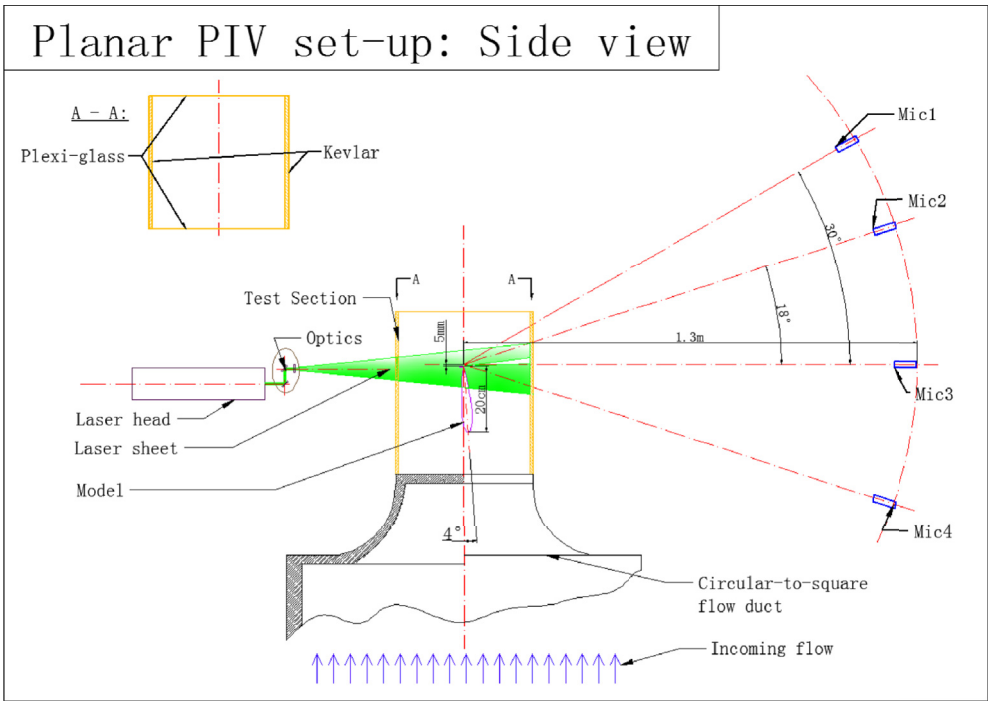

Fig. 3. Schematic of set-up for synchronized planar PIV and microphone measurements.

the speed of sound, and r, the modulus of the vector pointing from the source to the listener, namely, $t_e = t - r/c_0$.

$$p_a(\mathbf{x}, t) = -\frac{x_j}{4\pi c_0 |\mathbf{x}|} \frac{\partial}{\partial t} \int_{\delta V_y} \frac{p' \delta_{ij}}{r} |_{t_e = t - r/c_0} n_i dS, \tag{1}$$

In Eq. (1), x_j is the j^{th} component of the position vector $\mathbf{x}$, δ_{ij} is the Kronecker delta, dS indicates integral along the surface, and n_i is the surface normal vector.

When the solid body satisfies the compact body assumption $2\pi L/\lambda = He << 1$, where the Helmholtz number He characterizes the compactness, with L characteristic size of the body and λ the acoustic wavelength. Under this condition, a uniform value for retarded time $t_e = t - R/c_0$, with R the distance between listener and noise source, can be assumed for the sources distributed on the solid surface. Thus, the integral of pressure can be substituted by the instantaneous aerodynamic loads

Table 1
Parameters for synchronized planar PIV and microphone measurements.

Parameter	Value	Unit
Field of View (FOV), for each camera	80×80	mm^2
Field of View (FOV), combined	80×140	mm^2
Sensor size	704×704	pxs
Magnification factor, M	0.176	–
Focal length, f	105 (both cameras)	mm
Numerical aperture, $f_{\#}$	2.8 (both cameras)	–
PIV acquisition frequency, f_s	5	kHz
Pulse separation, dt	50	μs
Number of images, N	5773	–
Microphone placement (distance from the trailing edge)	1.3	m
Microphone acquisition frequency, f_{mic}	51.2	kHz

$F_j(t_e) = \int_{\delta V_y} p' \delta_{ij}|_{t_e=t-r/c_0} n_i dS$ [28]:

$$p'(\mathbf{x}, t) = -\frac{R_j}{4\pi c_0 R^2} \frac{\partial F_j(t_e)}{\partial t} \tag{2}$$

Eq. (2) is known as the Gutin's principle for compact and rigid body [28], where R_j is the j^{th} component of the position vector originating from the compact body pointing to the listener.

Eqs. (1) and (2) are referred to as the 'distributed' and the 'compact' formulations of Curle's analogy, respectively.

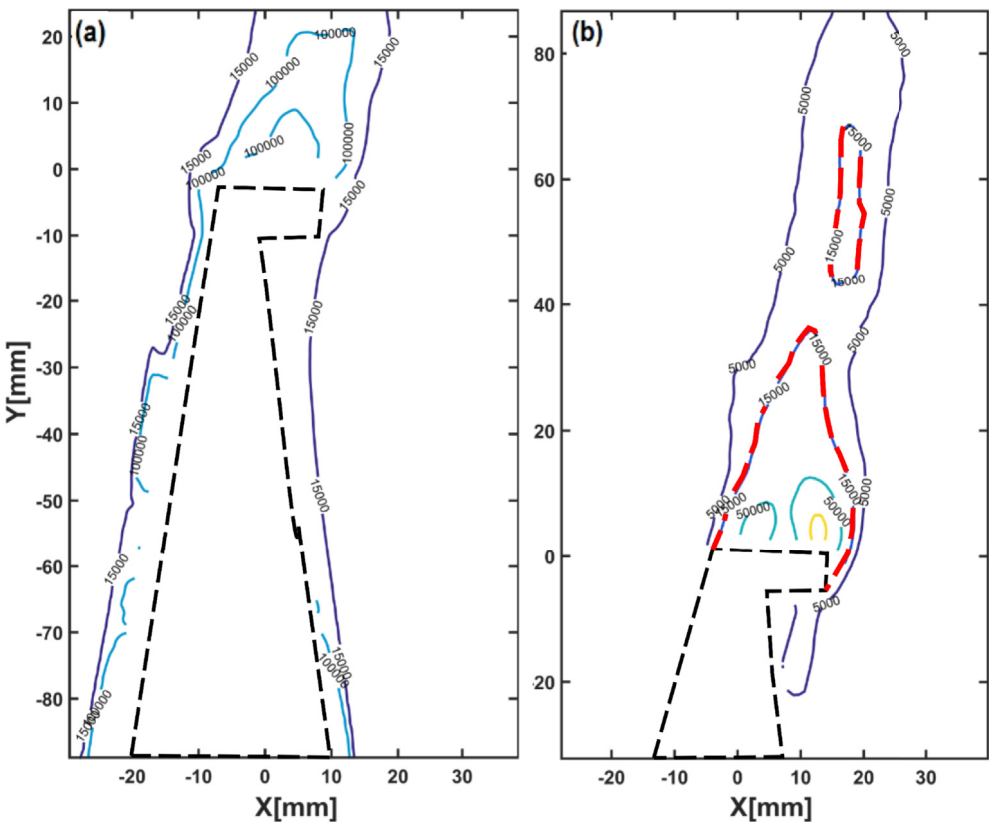

Fig. 4. Contours of time-averaged enstrophy $\overline{\varepsilon}$ of FOV 1(a) and FOV 2(b).

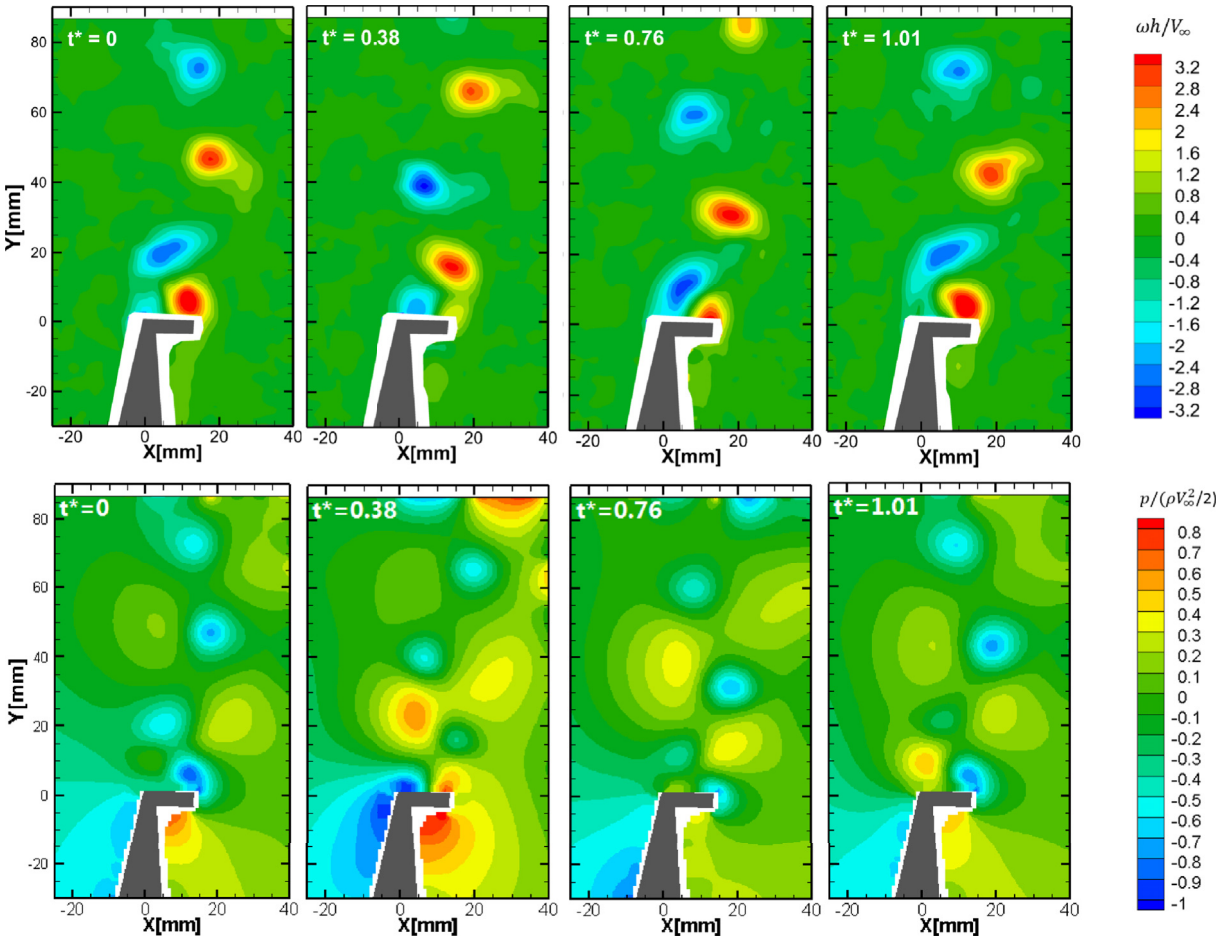

Fig. 5. Time sequence of the instantaneous vorticity (first row) and reconstructed pressure (second row) fields at normalized time instant $t^* = t/T_{shed}$ during approximately one shedding cycle.

3.2. Pressure reconstruction

The applications of Eq. (1) requires the pressure distribution on the airfoil. The pressure is related to the velocity by the Navier-Stokes equations (Eq. (3)):

$$\rho\frac{D\mathbf{v}}{Dt} = \rho\frac{\partial\mathbf{v}}{\partial t} + \rho\mathbf{v}\cdot\nabla\mathbf{v} = -\nabla p + \nabla\cdot\sigma, \tag{3}$$

and the spatial gradients of pressure can be expressed in either the Eulerian or the Lagrangian formulation (Eq. (4)):

$$\nabla p = -\rho\left(\frac{\partial\mathbf{v}}{\partial t} + (\mathbf{v}\cdot\nabla)\mathbf{v} - \nu\nabla^2\mathbf{v}\right) = -\rho\left(\frac{D\mathbf{v}}{Dt} - \nu\nabla^2\mathbf{v}\right) \tag{4}$$

where $D/Dt = \partial/\partial t + \mathbf{v}\cdot\nabla$ is the material derivative, ρ is the fluid density, $\mathbf{v}$ the velocity vector, p the static pressure and σ the viscous stress tensor.

By taking the in-plane divergence of Eq. (4), the equations can be rearranged into a form of the Poisson equation:

$$\frac{\partial^2 p}{\partial x^2} + \frac{\partial^2 p}{\partial y^2} = -\rho f_{xy} \tag{5}$$

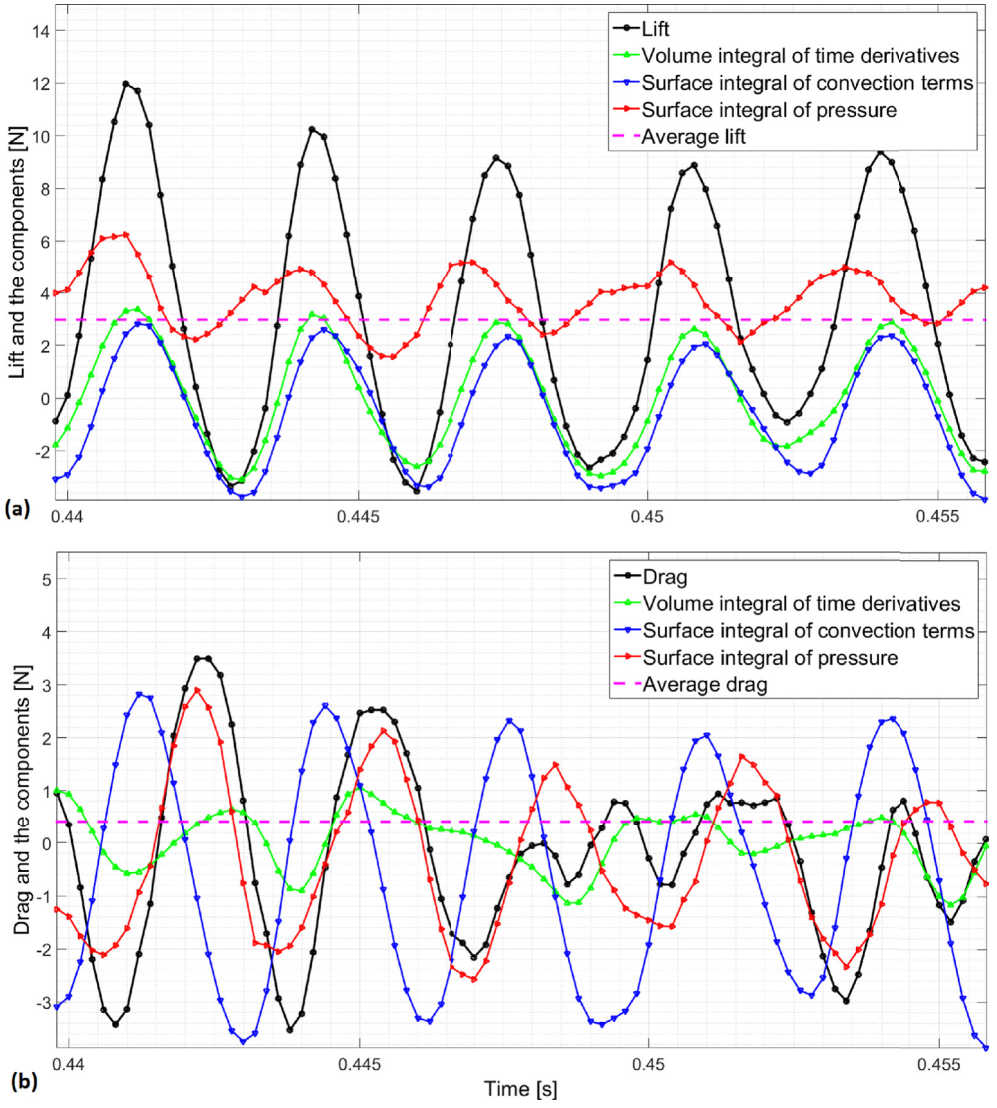

Fig. 6. Time series of lift(a), drag(b) and their respective components evaluated from PIV measurements of FOV2.

where the source term f_{xy} is a function of velocity and can be decomposed into the components of 2D and 3D. For high Reynolds number, the viscous term σ in Eq. (3) can be neglected [29], resulting in Eq. (6):

$$\begin{aligned} f_{xy} &= f_{2D} + f_{3D} \\ &= \left[\left(\frac{\partial u}{\partial x} \right)^2 + 2 \frac{\partial v}{\partial x} \frac{\partial u}{\partial y} + \left(\frac{\partial v}{\partial y} \right)^2 \right] \\ &+ \left[\frac{\partial (\nabla_{xy} \cdot \mathbf{v})}{\partial t} + (\mathbf{v} \cdot \nabla)(\nabla_{xy} \cdot \mathbf{v}) + \frac{\partial w}{\partial x} \frac{\partial u}{\partial z} + \frac{\partial w}{\partial y} \frac{\partial v}{\partial z} \right] \end{aligned} \tag{6}$$

For planar PIV measurements such as in the present case, knowledge of the spanwise velocity component is not available. Through the assumption of perfect spanwise coherence extending over the entire span, strictly applicable for quasi-2D laminar flows, the source term reduces to:

$$f_{xy} = \left(\frac{\partial u}{\partial x} \right)^2 + 2 \frac{\partial v}{\partial x} \frac{\partial u}{\partial y} + \left(\frac{\partial v}{\partial y} \right)^2 \tag{7}$$

As shown in Eq. (7), the source term is a combination of spatial velocity gradients. However, the velocity fields retrieved from the planar PIV measurement in the region directly downstream of the Gurney flap contain large measurement errors due to the

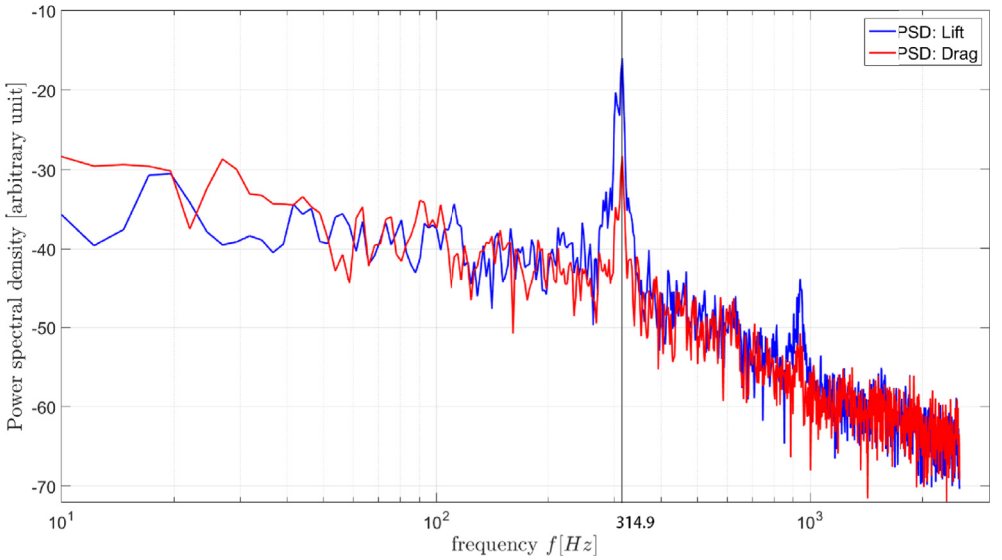

Fig. 7. Power spectra ($\Delta f = 2.4$ Hz) of lift and drag evaluated from PIV measurements of FOV2.

presence of high intensity 3D motion. The associated velocity gradients result in errors in the source term and in the solution of the Poisson equation. To reduce the effect of random measurement errors on the velocity gradients, the velocity field was smoothened with a Gaussian filter kernel, with a standard deviation of 10 vector pitches and a window size of 10 by 10 pixels.

The outer boundary of the domain is divided into a 'viscous region' (inside the wake) and an 'inviscid region' (outside of the wake) as proposed by Kurtulus et al. [21]. The criterion applied in this case is the local value of enstrophy, defined as:

$$\varepsilon = |\boldsymbol{\omega}|^2, \tag{8}$$

where $\boldsymbol{\omega}$ is the local vorticity. Fig. 4 shows the contours of the time-averaged enstrophy of the two FOVs.

For the velocity fields derived from the PIV measurements based on FOV 2, the threshold for the viscous region is set to $\varepsilon > 1.5 \times 10^4$ s^{-2}, corresponding to the enstrophy value evaluated at one wavelength of the vortex shedding mode downstream of the airfoil trailing edge (dashed line in Fig. 4(b)). Dirichlet boundary conditions are assigned to the inviscid region of the boundary, where pressure is estimated using Bernoulli's equation [30]:

$$p = P_\infty + \frac{1}{2}\rho V_\infty^2 - \frac{1}{2}\rho(u^2 + v^2) \tag{9}$$

Neumann boundary conditions are assigned to the airfoil surface and to the viscous region of the outer boundary. The pressure gradient in the Neumann condition is defined as in Eq. (4).

The velocity field measured by PIV based on FOV 1 is also smoothened with the Gaussian kernel filter as for the case of FOV 2, with standard deviation set to 10 vector pitches and window size of 10 by 10 pixels. However, in this case, the threshold for viscous region is set to $\varepsilon > 2 \times 10^5$ s^{-2}, evaluated from the order of magnitude of the maximum time-averaged enstrophy. The reason for increasing the threshold is to guarantee the extent of the Dirichlet boundary condition to prevent numerical instabilities in solving the Poisson equation.

3.3. Integral loads evaluation

The general integral form of the momentum balance is written as [30]:

$$\mathbf{F}(t) = -\rho \iiint_{\mathcal{V}} \frac{\partial \mathbf{v}}{\partial t} d\mathcal{V} - \rho \iint_{\delta\mathcal{V}} (\mathbf{v}\cdot\mathbf{n})\mathbf{v} dS - \iint_{\delta\mathcal{V}} p\mathbf{n} dS + \iint_{\delta\mathcal{V}} \boldsymbol{\tau}\mathbf{n} dS \tag{10}$$

Table 2
Statistics of the retarded time difference $t - t_e$ for microphones with respect to the distributed source locations on the airfoil surface (values given in [ms]).

Listener	min.$(t-t_e)$	max.$(t-t_e)$	mean.$(t-t_e)$	max.$(\Delta(t-t_e))$
Microphone 1	4.3	4.4	4.4	0.1
Microphone 2	4.0	4.0	4.0	0
Microphone 3	3.8	3.9	3.8	0.1
Microphone 4	3.9	4.0	4.0	0.1

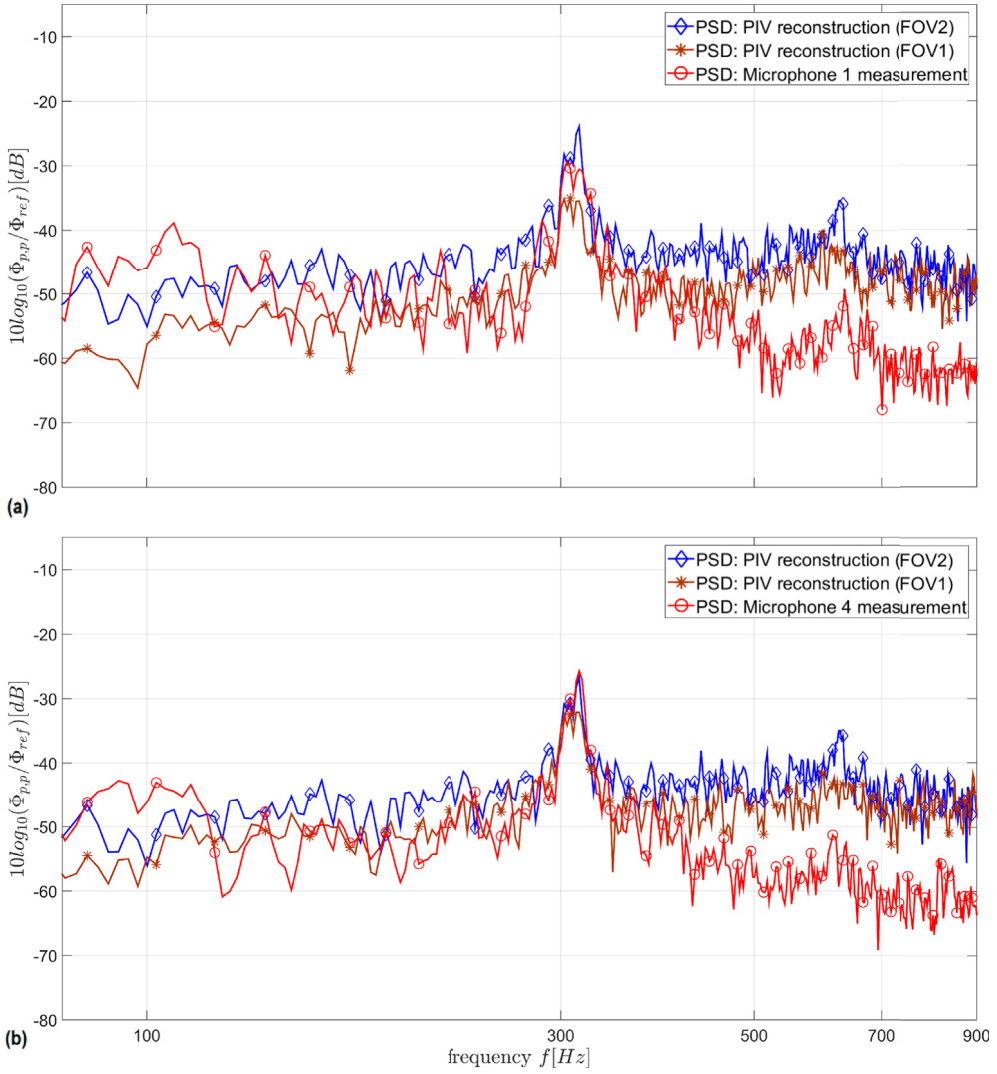

Fig. 8. Power spectra ($\Delta f = 2.4$ Hz) of far-field acoustic pressure evaluated by distributed formulation of Curle's analogy from PIV measurements of FOV1 and FOV2 based on full span coherence assumption in comparison with the simultaneous microphone measurement at the locations of Microphone 1 (a) and Microphone 4 (b). Reference value $\Phi_{ref} = 1\ \mathrm{Pa}^2 \cdot \mathrm{s}$.

In this case the planar PIV measurement cannot resolve the out-of-plane velocity, and therefore only the velocity components along the measurement plane x-y are considered. In addition, with the outer boundary of the control volume sufficiently far from the body surface, the viscous effects are neglected, resulting in:

$$\begin{bmatrix} D \\ L \end{bmatrix} = -\rho \iint_V \begin{bmatrix} \frac{\partial u}{\partial t} dxdy \\ \frac{\partial v}{\partial t} dxdy \end{bmatrix} + \rho \oint_S \begin{bmatrix} -u^2 dy + uvdx \\ uvdy + v^2 dx \end{bmatrix} + \oint_S \begin{bmatrix} -pdy \\ pdx \end{bmatrix} \tag{11}$$

Kurtulus et al. [21] also proposed a robust procedure for the evaluation of the pressure terms on the control surface in Eq. (11). As shown in Fig. 2 of reference [21], the part of the control surface wetted by the wake is defined as 'viscous region', where pressure is obtained by integrating Eq. (4), but neglecting the viscous contribution. To minimize the effect of error propagation in the process of spatial integration, outside of the wake, the pressure is estimated using Bernoulli's equation. In this way, the pressure in the wake region can be resolved by integrating from both edges of the wake, and the end point of integration, located in the inviscid region, can be compared with the value given by Bernoulli's equation. The difference between the results from the two approaches can then be considered as a residual and redistributed along the viscous region with a linear weighting function. The above-mentioned technique is applied to the incompressible scenario. The threshold for the viscous region was also set to $\epsilon > 1.5 \times 10^4\ \mathrm{s}^{-2}$.

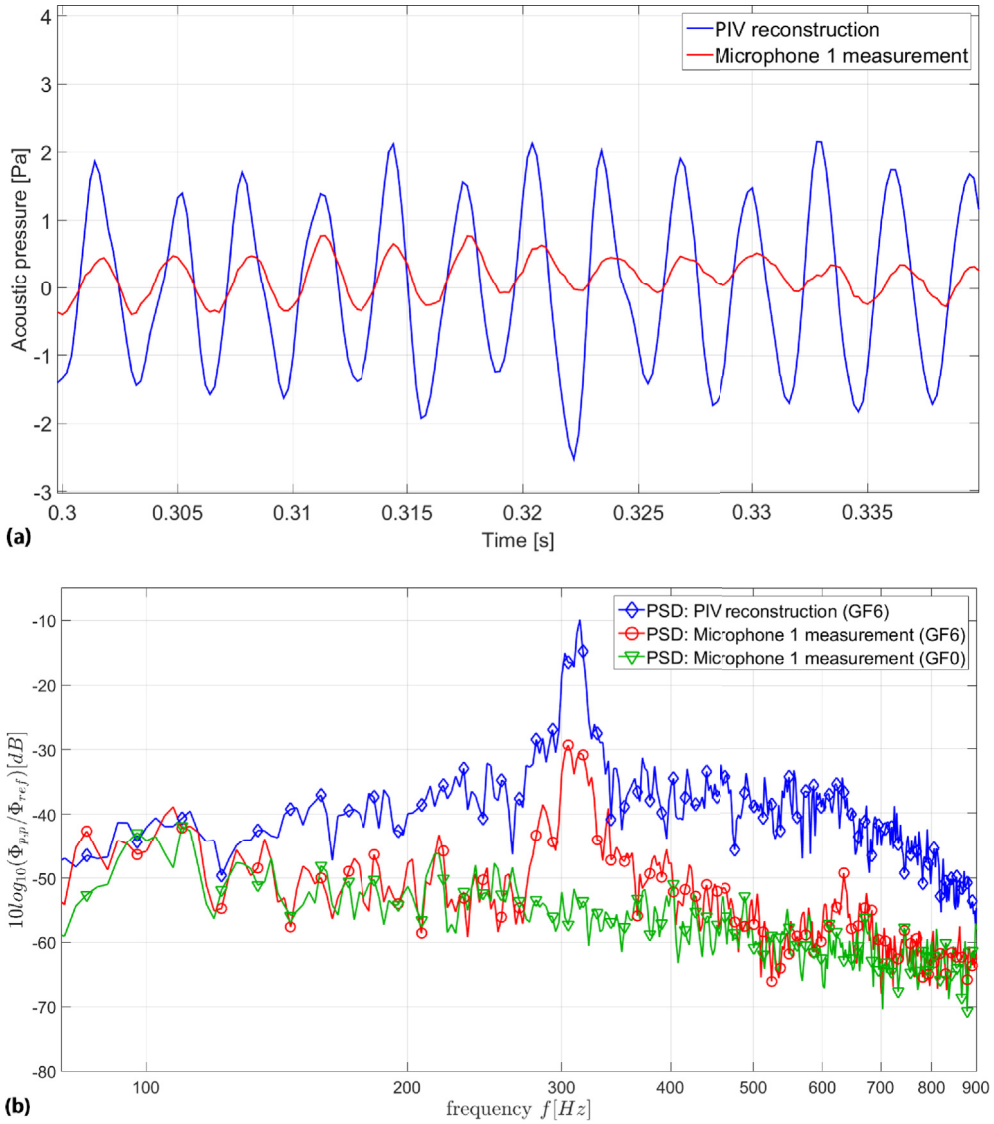

Fig. 9. Time series (a) and power spectra with $\Delta f = 2.4$Hz (b) of far-field acoustic pressure evaluated by compact formulation of Curle's analogy based on full span coherence assumption from PIV measurements in comparison with the simultaneous microphone measurement at the location of Microphone 1. The reference value $\Phi_{ref} = 1$ Pa$^2 \cdot$ s. GF6: 6% c Gurney flap mounted on the trailing edge. GF0: clean NACA 0015 configuration (no Gurney flap).

The application of the method requires that the upstream and side edges should locate sufficiently far-away from the solid surface, in order to assign $p = p_\infty$ on these three boundaries. In the experiments of the present study, the upstream edge of the field of view was placed at the location where the velocity fluctuation is negligible compared to that in the flow around the Gurney flap. In this way, Eq. (11) is applicable in estimating the fluctuating aerodynamic loads, which directly related to the emission of far-field noise.

4. Results and discussion

4.1. Instantaneous flow fields

In Fig. 2, in the wake region downstream of the Gurney flap, a deficit in the streamwise velocity component can be observed, and the alternation of positive and negative transverse velocity indicates the existence of large vortical structures. Correspondingly, the counter-rotating vortices can be observed from the time sequence of instantaneous vorticity fields in Fig. 5 (first row), illustrated by the coherent regions marked in red (counter-clockwise) and blue (clockwise). The vortices, which are shed at the trailing edge, are convected downstream at an average spacing of 5 cm and with a velocity of around 16.7 m $\cdot$ s^{-1}, which is approximately 83% of the free stream velocity. The spectral analysis of the fluctuating velocity depicts a peak frequency at 314.9

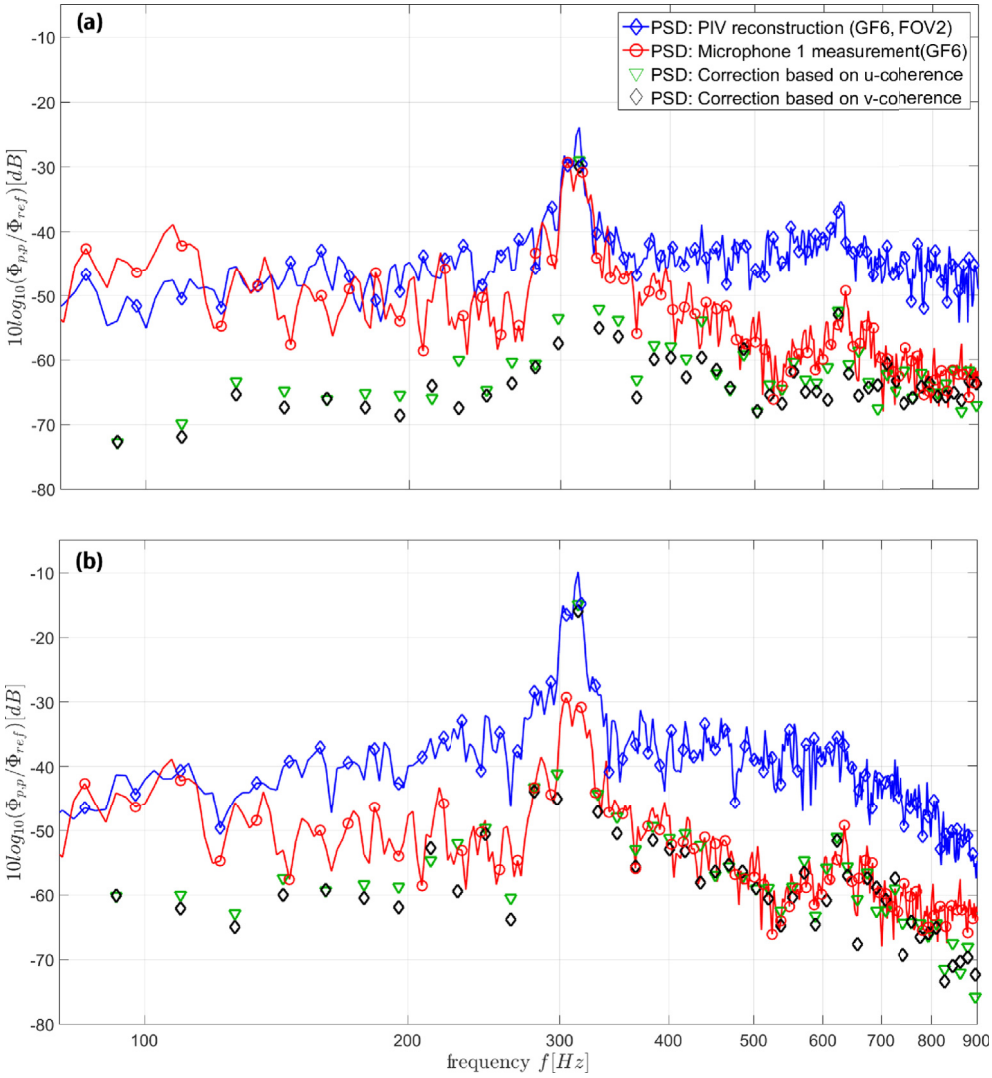

Fig. 10. Comparison of the computed spectra based on full span coherence assumption and on measured spanwise coherence length with the microphone measurements. (a) Distributed formulation, (b) Compact formulation.

Hz, corresponding to a period of $T_{shed} = 0.32$ ms.

The sequence of the snapshots of instantaneous pressure fields corresponding to the previously shown velocity and vorticity is presented in Fig. 5 (second row). The pressure downstream of the Gurney flap exhibits a coherent pattern as well as a distinguishable convection process similar to that present in the vorticity field. The locations of the local minima of the pressure coincide with the locations of the vortex cores as shown in Fig. 5, while the local maxima indicate the stagnation region caused by flow impinging on the solid surface (upstream of the Gurney flap) or the interaction of the vortices (downstream of the Gurney flap).

4.2. Aerodynamic loads

Fig. 6 shows the time series of lift and drag, with the aerodynamic loads and the three source terms in Eq. (11) plotted. The plots also show the mean value of the aerodynamic loads.

Periodicity can be observed in the reconstructed aerodynamic loads and the individual components. For lift, the fluctuations are primarily attributed to the volume integral of the time derivatives of the velocity and the surface integral of the convection terms, while for the drag, the major components are the two surface integral terms. However, it would be inaccurate to neglect any of the three components in both lift and drag, when looking closely at the order of magnitude and considering their

contribution to the phase of the overall fluctuation.

The resulting power spectra of the aerodynamic loads evaluated from the PIV measurement on FOV 2 are presented in Fig. 7. Both the lift and the drag peak at the frequency of 314.9 Hz, which is consistent with the shedding frequency as expected.

4.3. Acoustic prediction

4.3.1. Acoustic prediction with distributed formulation of Curle's analogy

As shown in Eq. (1), the pressure fluctuation at the location of the listener (or microphone) is the sum of the contributions received at time instant t and emitted at (different) retarded time instant(s) t_e over the source region. Therefore, information about the retarded time for each source location is required before integrating the distributed source.

Since the listener location is fixed, the value $t - t_e = r/c_0$ is a constant over time for each location in the source field for a certain listener. The values of $t - t_e$ for this case are evaluated for the solid surface locations within the PIV field of view and are summarized in Table 2.

It can be observed that the largest difference in retarded time is 0.1 ms along the surface of airfoil. Under the sampling rate of the PIV measurements (5 kHz), the time interval between two snapshots of velocity field is 0.2 ms. For the source locations with a different retarded time from the mean value, the treatment can either be interpolation of the local time series of pressure to obtain the value in between the two snapshots, or approximating with the value of the nearest snapshot in time.

With further observation of the mean value of $(t - t_e)$, it can be inferred that source locations with a value of $(t - t_e)$ that deviates as much as 0.1 ms (half the interval between two PIV snapshots) from the mean value only account a small portion of airfoil surface. The observation of retarded time provides further evidence that the experimental set-up for the current study satisfies the compact source assumption, and thus each microphone can be assigned with the respective mean value of $(t - t_e)$ for the calculation of retarded time.

The rigorous application of Eq. (1) requires the time derivative of the pressure all around the airfoil. However, since the flow on the leading edge of the airfoil is approximately steady compared to that around the trailing edge (the root mean square of the velocity fluctuations on the pressure surface at $0.8c$ is one order of magnitude lower than that around the Gurney flap), it is possible to compute the surface integral in equation (3) only in a region close to the Gurney flap. As a consequence, knowledge of the time derivative of the surface pressure $\partial p/\partial t$ is required only close to the Gurney flap and not in the leading edge region.

The resulting power spectra of the acoustic prediction based on the PIV measurement on FOV 2 are presented in Fig. 8. As comparison, the measurements with the corresponding microphones are plotted on the same schematic. The spectra of microphone measurements and the acoustic prediction all feature a local peak at 315 Hz in agreement with the vortex shedding frequency, with the variability of the peak frequency being less than 10 Hz. The first harmonic at 630 Hz can be observed but is not evident for microphone measurements, yet it is more noticeable on the spectra predicted from the PIV measurements. For the noise prediction based on the PIV measurement using FOV 1, the sound pressure level at the peak frequency is slightly over-estimated by the PIV measurement for listener locations at microphone 1, 2 and 3 (the results of listener locations 2 and 3 are not shown). The over-estimation in sound pressure level can be attributed to the 2D flow assumption, or assumption of perfect spanwise coherence. However, the over-estimation in sound pressure level is not observed for microphone 4. Thus, the latter assumption is only one of the contributing factors (though an important one) that may influence the prediction of the sound pressure level. The reduction in the estimated sound pressure level can possibly be ascribed to:

- The omission of velocity/pressure fluctuations on the airfoil surface upstream of FOV 2.
- The damping of fluctuation amplitude due to smoothing of the velocity field.

To reduce the influence of the two above-mentioned factors, one can either move the field of view upstream, or avoid the smoothing of the velocity field by applying the compact formulation of Curle's analogy. The viability of the former is evaluated by applying the distributed Curle's analogy to the PIV measurements based on FOV 1, the results of which are presented in the following paragraphs of this section, while the latter is discussed in 4.3.2.

Fig. 8 also presents the resulting power spectra of the acoustic prediction based on the PIV measurement on FOV 1. Instead of yielding a higher sound pressure level than the prediction made from FOV 2, the sound pressure level predicted from FOV 1 is lower. This reduction in amplitude of pressure fluctuations can be attributed to the arbitrary increase in the enstrophy threshold. The extra Dirichlet boundary condition assigned to the outer boundary, while stabilizing the solution, also exerts a damping effect on the fluctuations.

It can be observed that moving the PIV field of view upstream, while maintaining the spatial resolution (and hence the size of the field of view), is not favorable for pressure reconstruction, since at the downstream edge the physical domain is submerged in the near-wake of the Gurney flap, thus invalidating the choice of boundary conditions and exacerbating the errors in the solution. The amplitude of the computed acoustic spectra does not decay in the high frequency range as in the spectra of microphone measurements. The discrepancy is partially ascribed to the short spanwise coherence length of the high frequency component away from the tonal component. The flow motions in this frequency range are dominated by the 3D effect, and thus the 2D assumption is less applicable, leading to overestimations. The discussions regarding the spanwise coherence length are detailed in 4.3.3 and Appendix. A similar flat spectra observed in the higher frequency range of transverse velocity fluctuations (Fig. 2(c)) indicates that the more pronounced difference in acoustic spectra at higher frequency is attributed to the increased noise level. This increase in measurement noise is due to the limited dynamic velocity range of PIV measurements, since the

wavelength of velocity fluctuations associated to higher frequency is shorter.

4.3.2. Acoustic prediction with FOV 2-based compact formulation

Based on the aerodynamic loads evaluated from the PIV measurement, Eq. (2) is implemented for FOV 2 to reconstruct the far-field acoustic pressure. Due to the errors introduced by increasing the enstrophy threshold discussed in 4.3.1, the application of compact Curle's analogy on the PIV measurements with FOV 1 is left out of the discussion. To avoid the spurious error in the time derivatives of the instantaneous aerodynamic loads caused by the measurement noise, a Savitzky-Golay filter with a second order polynomial over a window size of 9 consecutive time instants was applied to the time series of the reconstructed aerodynamic loads. The distance from the airfoil trailing edge and each respective microphone was used to calculate the uniform retarded time.

Time series of the far-field acoustic pressure, both from the microphone measurements and from the PIV reconstruction based on the perfect spanwise coherence assumption, are shown in Fig. 9 (a). The two measurements roughly share the same period and phase. However, the maximum value obtained from the cross-correlation coefficient of the far-field pressure measured by microphone and that evaluated by PIV is barely 0.19. This low value in cross-correlation coefficients can be the result of the assumption of perfect spanwise coherence, which essentially regards the signal measured at the mid-span location representative of the signals over the entire span. Since the far-field acoustics is a result of the integration of surface pressure fluctuations over the entire span, a smaller spanwise coherence degrades the correlation. In addition, wall reflections that result in interferences in the non-anechoic environment may also degrade the level of correlation.

As expected, the amplitude predicted from the data acquired in the PIV measurements is larger than that measured by the microphones at all four locations, since in reality the flow is intrinsically 3D and the spanwise coherence length is shorter than the wing span.

Fig. 9 (b) shows the power spectra of the far-field acoustic pressure. The acoustic spectra acquired respectively through the predictions of PIV with the application of the compact formulation and the measurements of microphones both present a peak at a frequency of around 315 Hz. A peak of the same frequency has been observed in the spectra (Fig. 8) given by the distributed formulation of Curle's analogy (Eq. (1)) and is in consistent with that of aerodynamic loads. Fig. 9 (b) also presents the acoustic spectra of the clean NACA 0015 (no Gurney flap on the airfoil trailing edge). The absence of the peak of the tonal frequency on the power spectra of a NACA 0015 without Gurney flap provides an additional indication that the tonal noise generated by the GF6 model should be attributed to the presence of the Gurney flap.

4.3.3. Correction based on spanwise coherence

The power spectra of the reconstructed far-field noise from 2D-PIV measurements presented in 4.3.1 and 4.3.2 are based on the assumption of perfect spanwise coherence, which extrapolate the 2D velocity data along the entire span. With the distributed formulation of Curle's analogy, this extrapolation yields overestimations of around 6 dB in Sound Pressure Level (SPL) at tonal frequency 315 Hz, and 15 dB for its second harmonic 630 dB. Conversely, with the compact formulation, the overestimations in tonal frequency and high frequency components are 17 dB and 22 dB, respectively.

To account for the spanwise coherence in pressure fluctuations, a coherence weighted amplitude correction based on stereoscopic PIV measurements (see Appendix) was carried out following the method proposed by Kato et al. [31]. The method was proven to work reasonably well by literature such as [13,32].

The triangles and diamonds in Fig. 10 represent the corrected SPL based on the spanwise coherence estimated from transverse (u-component) and streamwise (v-component) velocity, respectively. For the distributed formulation, the coherence weighted amplitude correction lowers the overestimation at the tonal frequency to around 2 dB, and to around 1 dB at the second harmonic. For the compact formulation, the correction lowers the overestimation at the tonal frequency to around 12 dB, and around 8 dB at second harmonic. These indicate an amplitude reduction of 4 dB and 14 dB for first and second harmonics, respectively, compared to the perfect coherence case. For both formulations of Curle's analogy, the coherence weighted amplitude correction brings the high frequency components into good agreements with microphone measurements.

5. Conclusion

In the present study, the feasibility of acoustic evaluation of high-lift devices based on the time-resolved PIV velocity measurements was investigated. The investigation was performed on a NACA 0015 airfoil with a Gurney flap of the height of 6% the chord length.

The velocity fields measured by TR-PIV around and downstream of the Gurney flap were used to reconstruct the pressure field by means of the solution of the in-plane Poisson equation. Coherence pattern and distinguishable convection can be observed downstream of the Gurney flap in the reconstructed pressure field. In addition the locations of the local minima of the reconstructed pressure are consistent with the locations of vortex cores identified in the vorticity field. The evaluated pressure distribution on the airfoil surface constitutes the source terms in the 'distributed' formulation of Curle's analogy. Alternatively, a more robust integral approach based on the evaluation of instantaneous aerodynamic loads, namely the 'compact' formulation, was followed to offer a comparison. The results from both approaches were compared with the far-field microphone measurements at corresponding locations obtained simultaneously with the PIV measurement. The frequency of the tonal noise is consistent with the frequency of vortex shedding. The power spectra of the fluctuations of velocity, aerodynamic loads and

far-field pressure did not indicate the existence of a second shedding mode for this configuration as the one proposed by Troolin et al. [33].

The noise prediction using the 'distributed' formulation of Curle's analogy based on perfect spanwise coherence assumption shows good agreement with the microphone measurement in terms of frequency around the first harmonic, and the amplitude agrees within 5 dB. The spectral components predicted by the 'compact' formulation shows similar results, however, the overestimation in SPL is comparatively large. However, the 'compact' formulation is relatively robust in the experimental point of view, since the evaluation of the surface pressure involved in the 'distributed' formulation is susceptible to the spurious in-plane velocity fluctuation caused by the strong 3D motions direct downstream of the trailing edge. The application of coherence weighted amplitude correction brings the predicted amplitudes of high frequency components in to excellent agreement with the microphone measurements for both formulations.

Acknowledgement

The three authors were affiliated to Delft University of Technology, the Netherlands, whilst the experimental study was carried out.

Appendix. Spanwise coherence measurements

In the present study, the frequency dependent spanwise coherence length was measured with stereoscopic PIV at a free-stream velocity of 20 $m \cdot s^{-1}$. The field of view was a 70×70 mm^2 shaped square in the streamwise-spanwise plane (x-z) 5 mm downstream the airfoil trailing edge (Fig. 11).

The visualization of the streamwise velocity presents the vortical coherent structures. The spanwise coherence of fluctuating velocities was calculated according to the definition of Eq. (12), where $\widehat{u}'$ signifies the complex component of the Fourier transform of velocity component u or v, and z_0 was chosen as the mid-span location. The spanwise coherence was calculated along the lines parallel to the airfoil trailing edge, on which the maximum RMS of velocity fluctuations reaches maxima. For u and v component, the locations were $x = 13$ mm and 17 mm, respectively.

$$\gamma^2(z,f) = \frac{|\langle \widehat{u}'(z_0,f)\widehat{u}'^*(z,f)\rangle|^2}{|\langle \widehat{u}'(z_0,f)\widehat{u}'^*(z_0,f)\rangle \langle \widehat{u}'(z,f)\widehat{u}'^*(z,f)\rangle|} \tag{12}$$

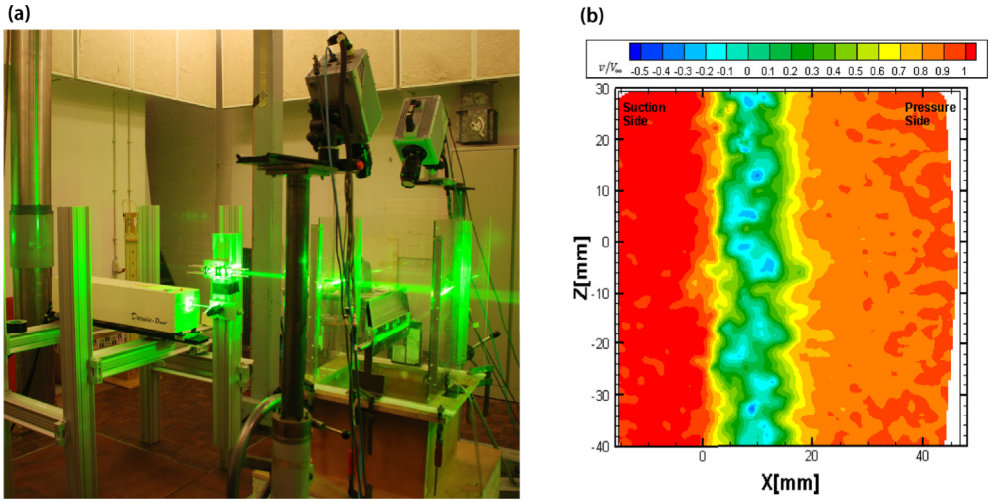

Fig. 11. Experimental setup for spanwise coherence length measurements (a) and a snapshot of instantaneous streamwise velocity component in the streamwise-spanwise plane(x-z) 5 mm downstream of the airfoil trailing edge (b).

For each frequency component, a Gaussian function is fitted around $z = z_0$ for coherence coefficients and spanwise locations. The frequency dependent coherence length $l(f)$ is defined here as the width of the Gaussian curve at $\gamma = e^{-2}$. The tonal frequency features the largest coherence length, corresponding to 14 cm and 10.5 cm respectively for streamwise and transverse components. The coherence length drops sharply above the tonal frequency, with a local maxima at the second harmonic, corresponding to 4 cm and 2.1 cm for streamwise and transverse components.

$N = L/l(f)$ uncorrelated spanwise segments contributes to the overestimation in the 2D acoustic prediction presented in 4, where L signifies the span of the airfoil model. Which corresponds to applying a correction term $-10\log(L/l)$ to the perfect

spanwise coherence prediction [13].

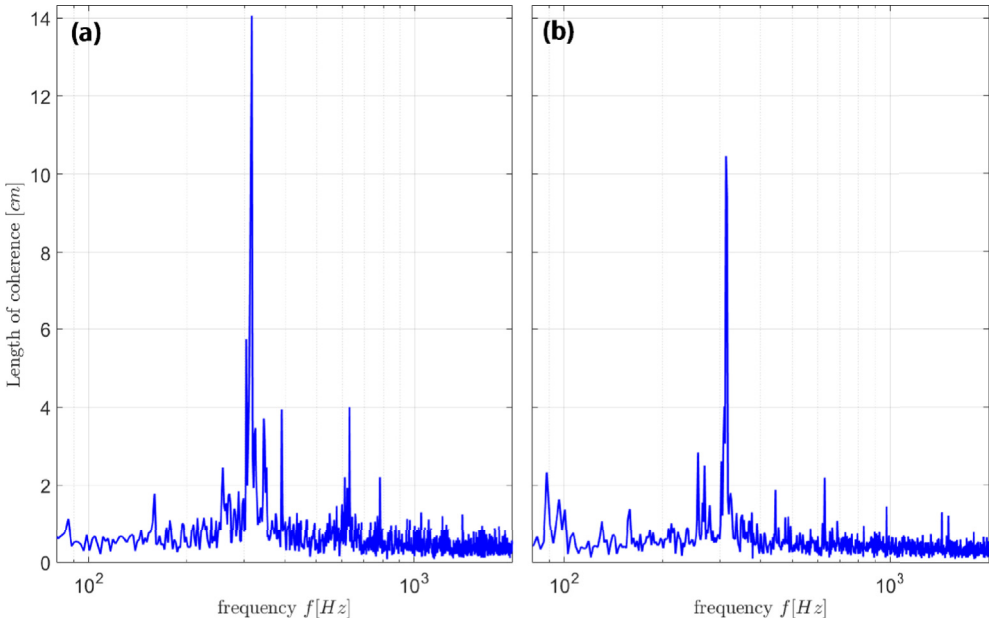

Fig. 12. Spanwise coherence length calculated based on transverse (u-component) (a) and streamwise (v-component) (b) velocity.

References

[1] M. Roger, Aeroacoustics: some theoretical background – the acoustic analogy noise from moving surfaces, in: Course, Computational Aeroacoustics; Rhode Saint Genese, Belgium.
[2] F. Hutcheson, T. Brooks, Effects of angle of attack and velocity on trailing edge noise determined using microphone array measurements, Int. J. Aeroacoustics 5 (2006) 39–66.
[3] D. Casalino, M. Jacob, M. Roger, Prediction of rod-airfoil interaction noise using the Ffowcs-Williams-Hawkings analogy, AIAA J. 41 (2003) 182–191.
[4] M. J. Lighthill, On sound generated aerodynamically i general theory, in: Proceedings of the Royal Society of London a: Mathematical, Physical and Engineering Sciences, vol. 211, The Royal Society, pp. 564–587.
[5] A. Henning, K. Kaepernick, K. Ehrenfried, L. Koop, A. Dillmann, Investigation of aeroacoustic noise generation by simultaneous particle image velocimetry and microphone measurements, Exp. Fluid 45 (2008) 1073–1085.
[6] A. Henning, L. Koop, K. Ehrenfried, Simultaneous particle image velocimetry and microphone array measurements on a rod-airfoil configuration, AIAA J. 48 (2010) 2263–2273.
[7] A. Henning, A. Schröder, L. Koop, J. Agocs, Causality correlation analysis on a cold jet by means of simultaneous particle image velocimetry and microphone measurements, J. Sound Vib. 332 (2013) 3148–3162.
[8] A. Henning, B. Wrede, R. Geisler, Aeroacoustic investigation of a high-lift device by means of synchronized PIV and microphone measurements, in: 16th International Symposium on Applications of Laser Techniques to Fluid Mechanics, p. 1–11.
[9] S. Pröbsting, J. Serpieri, F. Scarano, Experimental investigation of aerofoil tonal noise generation, J. Fluid Mech. 747 (2014) 656–687.
[10] S. Pröbsting, F. Scarano, S.C. Morris, Regimes of tonal noise on an airfoil at moderate Reynolds number, J. Fluid Mech. 780 (2015) 407–438.
[11] C. Haigermoser, Application of an acoustic analogy to PIV data from rectangular cavity flows, Exp. Fluid 47 (2009) 145–157.
[12] V. Koschatzky, J. Westerweel, B. J. Boersma, Comparison of two acoustic analogies applied to experimental PIV data for cavity sound emission estimation, in: Proceedings of the 16th AIAA/CEAS Aeroacoustic Conference, p. 7–9.
[13] V. Lorenzoni, M. Tuinstra, F. Scarano, On the use of time-resolved particle image velocimetry for the investigation of rod–airfoil aeroacoustics, J. Sound Vib. 331 (2012) 5012–5027.
[14] S. Pröbsting, M. Tuinstra, F. Scarano, Trailing edge noise estimation by tomographic particle image velocimetry, J. Sound Vib. 346 (2015) 117–138.
[15] J. Shah, A. Sciacchitano, S. Pröbsting, Investigation of aeroacoustics and flow dynamics of a NACA 0015 airfoil with a gurney flap using TR-PIV, in: 18th Int Symp on Applications of Laser Techniques to Fluid Mechanics.
[16] T. Baur, J. Köngeter, PIV with high temporal resolution for the determination of local pressure reductions from coherent turbulence phenomena, in: 3rd International Workshop on Particle Image Velocimetry, Santa Barbara, CA, USA.
[17] R. Gurka, A. Liberzon, D. Hefetz, D. Rubinstein, U. Shavit, Computation of pressure distribution using PIV velocity data, in: Workshop on Particle Image Velocimetry, vol. 2.
[18] X. Liu, J. Katz, Instantaneous pressure and material acceleration measurements using a four-exposure PIV system, Exp. Fluid 41 (2006) 227–240.
[19] D. Violato, P. Moore, F. Scarano, Lagrangian and eulerian pressure field evaluation of rod-airfoil flow from time-resolved tomographic PIV, Exp. Fluid 50 (2011) 1057–1070.
[20] R. De Kat, B. Van Oudheusden, Instantaneous planar pressure determination from PIV in turbulent flow, Exp. Fluid 52 (2012) 1089–1106.
[21] D. Kurtulus, F. Scarano, L. David, Unsteady aerodynamic forces estimation on a square cylinder by TR-PIV, Exp. Fluid 42 (2007) 185–196.
[22] F. Noca, D. Shiels, D. Jeon, A comparison of methods for evaluating time-dependent fluid dynamic forces on bodies, using only velocity fields and their derivatives, J. Fluid Struct. 13 (1999) 551–578.
[23] W.J. Devenport, R.A. Burdisso, A. Borgoltz, P.A. Ravetta, M.F. Barone, K.A. Brown, M.A. Morton, The kevlar-walled anechoic wind tunnel, J. Sound Vib. 332 (2013) 3971–3991.
[24] J. Westerweel, Fundamentals of digital particle image velocimetry, Meas. Sci. Technol. 8 (1997) 1379.

[25] J. Westerweel, F. Scarano, Universal outlier detection for PIV data, Exp. Fluid 39 (2005) 1096–1100.
[26] M.E. Goldstein, Aeroacoustics, McGraw-Hill International Book Co., New York, 1976. , 1976. 305 p. 1.
[27] M. Wang, J.B. Freund, S.K. Lele, Computational prediction of flow-generated sound, Annu. Rev. Fluid Mech. 38 (2006) 483–512.
[28] A. Powell, Theory of vortex sound, J. Acoust. Soc. Am. 36 (1964) 177–195.
[29] B.W. van Oudheusden, F. Scarano, E.W. Roosenboom, E.W. Casimiri, L.J. Souverein, Evaluation of integral forces and pressure fields from planar velocimetry data for incompressible and compressible flows, Exp. Fluid 43 (2007) 153–162.
[30] J.D. Anderson Jr., Fundamentals of Aerodynamics, Tata McGraw-Hill Education, 2010.
[31] C. Kato, A. Iida, Y. Takano, H. Fujita, M. Ikegawa, Numerical prediction of aerodynamic noise radiated from low mach number turbulent wake, AIAA Pap. (1993) 93–145.
[32] R. Oreslli, J. R. Meneghini, F. Saltara, Two and three-dimensional simulation of sound generated by flow around a circular cylinder, in: 15th AIAA/CEAS Aeroacoustics Conference, AIAA, vol. 3270.
[33] D. Troolin, E. Longmire, W. Lai, Time resolved PIV analysis of flow over a NACA 0015 airfoil with gurney flap, Exp. Fluid 41 (2006) 241–254.